J/ψ suppression at forward rapidity in Au + Au collisions at $\sqrt{s_{NN}} = 200$ GeV

A. Adare,[11] S. Afanasiev,[27] C. Aidala,[40] N. N. Ajitanand,[57] Y. Akiba,[51,52] H. Al-Bataineh,[46] J. Alexander,[57] K. Aoki,[33,51] Y. Aramaki,[10] E. T. Atomssa,[34] R. Averbeck,[58] T. C. Awes,[47] B. Azmoun,[5] V. Babintsev,[22] M. Bai,[4] G. Baksay,[18] L. Baksay,[18] K. N. Barish,[6] B. Bassalleck,[45] A. T. Basye,[1] S. Bathe,[6] V. Baublis,[50] C. Baumann,[41] A. Bazilevsky,[5] S. Belikov,[5,*] R. Belmont,[62] R. Bennett,[58] A. Berdnikov,[54] Y. Berdnikov,[54] A. A. Bickley,[11] J. S. Bok,[65] K. Boyle,[58] M. L. Brooks,[36] H. Buesching,[5] V. Bumazhnov,[22] G. Bunce,[5,52] S. Butsyk,[36] C. M. Camacho,[36] S. Campbell,[58] C.-H. Chen,[58] C. Y. Chi,[12] M. Chiu,[5] I. J. Choi,[65] R. K. Choudhury,[3] P. Christiansen,[38] T. Chujo,[61] P. Chung,[57] O. Chvala,[6] V. Cianciolo,[47] Z. Citron,[58] B. A. Cole,[12] M. Connors,[58] P. Constantin,[36] M. Csanád,[16] T. Csörgő,[30] T. Dahms,[58] S. Dairaku,[33,51] I. Danchev,[62] K. Das,[19] A. Datta,[40] G. David,[5] A. Denisov,[22] A. Deshpande,[52,58] E. J. Desmond,[5] O. Dietzsch,[55] A. Dion,[58] M. Donadelli,[55] O. Drapier,[34] A. Drees,[58] K. A. Drees,[4] J. M. Durham,[58] A. Durum,[22] D. Dutta,[3] S. Edwards,[19] Y. V. Efremenko,[47] F. Ellinghaus,[11] T. Engelmore,[12] A. Enokizono,[35] H. En'yo,[51,52] S. Esumi,[61] B. Fadem,[42] D. E. Fields,[45] M. Finger Jr.,[7] M. Finger,[7] F. Fleuret,[34] S. L. Fokin,[32] Z. Fraenkel,[64,*] J. E. Frantz,[58] A. Franz,[5] A. D. Frawley,[19] K. Fujiwara,[51] Y. Fukao,[51] T. Fusayasu,[44] I. Garishvili,[59] A. Glenn,[11] H. Gong,[58] M. Gonin,[34] Y. Goto,[51,52] R. Granier de Cassagnac,[34] N. Grau,[12] S. V. Greene,[62] M. Grosse Perdekamp,[23,52] T. Gunji,[10] H.-Å. Gustafsson,[38,*] J. S. Haggerty,[5] K. I. Hahn,[17] H. Hamagaki,[10] J. Hamblen,[59] J. Hanks,[12] R. Han,[49] E. P. Hartouni,[35] E. Haslum,[38] R. Hayano,[10] M. Heffner,[35] T. K. Hemmick,[58] T. Hester,[6] X. He,[20] J. C. Hill,[26] M. Hohlmann,[18] W. Holzmann,[12] K. Homma,[21] B. Hong,[31] T. Horaguchi,[21] D. Hornback,[59] S. Huang,[62] T. Ichihara,[51,52] R. Ichimiya,[51] J. Ide,[42] Y. Ikeda,[61] K. Imai,[33,51] M. Inaba,[61] D. Isenhower,[1] M. Ishihara,[51] T. Isobe,[10,51] M. Issah,[62] A. Isupov,[27] D. Ivanischev,[50] B. V. Jacak,[58,†] J. Jia,[5,57] J. Jin,[12] B. M. Johnson,[5] K. S. Joo,[43] D. Jouan,[48] D. S. Jumper,[1] F. Kajihara,[10] S. Kametani,[51] N. Kamihara,[52] J. Kamin,[58] J. H. Kang,[65] J. Kapustinsky,[36] K. Karatsu,[33,51] D. Kawall,[40,52] M. Kawashima,[53,51] A. V. Kazantsev,[32] T. Kempel,[26] A. Khanzadeev,[50] K. M. Kijima,[21] B. I. Kim,[31] D. H. Kim,[43] D. J. Kim,[28] E. J. Kim,[8] E. Kim,[56] S. H. Kim,[65] Y. J. Kim,[23] E. Kinney,[11] K. Kiriluk,[11] Á. Kiss,[16] E. Kistenev,[5] L. Kochenda,[50] B. Komkov,[50] M. Konno,[61] J. Koster,[23] D. Kotchetkov,[45] A. Kozlov,[64] A. Král,[13] A. Kravitz,[12] G. J. Kunde,[36] K. Kurita,[53,51] M. Kurosawa,[51] Y. Kwon,[65] G. S. Kyle,[46] R. Lacey,[57] Y. S. Lai,[12] J. G. Lajoie,[26] A. Lebedev,[26] D. M. Lee,[36] J. Lee,[17] K. B. Lee,[31] K. Lee,[56] K. S. Lee,[31] M. J. Leitch,[36] M. A. L. Leite,[55] E. Leitner,[62] B. Lenzi,[55] P. Liebing,[52] L. A. Linden Levy,[11] T. Liška,[13] A. Litvinenko,[27] H. Liu,[36,46] M. X. Liu,[36] X. Li,[9] B. Love,[62] R. Luechtenborg,[41] D. Lynch,[5] C. F. Maguire,[62] Y. I. Makdisi,[4] A. Malakhov,[27] M. D. Malik,[45] V. I. Manko,[32] E. Mannel,[12] Y. Mao,[49,51] H. Masui,[61] F. Matathias,[12] M. McCumber,[58] P. L. McGaughey,[36] N. Means,[58] B. Meredith,[23] Y. Miake,[61] A. C. Mignerey,[39] P. Mikeš,[7,25] K. Miki,[51,61] A. Milov,[5] M. Mishra,[2] J. T. Mitchell,[5] A. K. Mohanty,[3] Y. Morino,[10] A. Morreale,[6] D. P. Morrison,[5] T. V. Moukhanova,[32] J. Murata,[53,51] S. Nagamiya,[29] J. L. Nagle,[11] M. Naglis,[64] M. I. Nagy,[16] I. Nakagawa,[51,52] Y. Nakamiya,[21] T. Nakamura,[21,29] K. Nakano,[51,60] J. Newby,[35] M. Nguyen,[58] R. Nouicer,[5] A. S. Nyanin,[32] E. O'Brien,[5] S. X. Oda,[10] C. A. Ogilvie,[26] K. Okada,[52] M. Oka,[61] Y. Onuki,[51] A. Oskarsson,[38] M. Ouchida,[21,51] K. Ozawa,[10] R. Pak,[5] V. Pantuev,[24,58] V. Papavassiliou,[46] I. H. Park,[17] J. Park,[56] S. K. Park,[31] W. J. Park,[31] S. F. Pate,[46] H. Pei,[26] J.-C. Peng,[23] H. Pereira,[14] V. Peresedov,[27] D.Yu. Peressounko,[32] C. Pinkenburg,[5] R. P. Pisani,[5] M. Proissl,[58] M. L. Purschke,[5] A. K. Purwar,[36] H. Qu,[20] J. Rak,[28] A. Rakotozafindrabe,[34] I. Ravinovich,[64] K. F. Read,[47,59] K. Reygers,[41] V. Riabov,[50] Y. Riabov,[50] E. Richardson,[39] D. Roach,[62] G. Roche,[37] S. D. Rolnick,[6] M. Rosati,[26] C. A. Rosen,[11] S. S. E. Rosendahl,[38] P. Rosnet,[37] P. Rukoyatkin,[27] P. Ružička,[25] B. Sahlmueller,[41] N. Saito,[29] T. Sakaguchi,[5] K. Sakashita,[51,60] V. Samsonov,[50] S. Sano,[10,63] T. Sato,[61] S. Sawada,[29] K. Sedgwick,[6] J. Seele,[11] R. Seidl,[23] A.Yu. Semenov,[26] R. Seto,[6] D. Sharma,[64] I. Shein,[22] T.-A. Shibata,[51,60] K. Shigaki,[21] M. Shimomura,[61] K. Shoji,[33,51] P. Shukla,[3] A. Sickles,[5] C. L. Silva,[55] D. Silvermyr,[47] C. Silvestre,[14] K. S. Sim,[31] B. K. Singh,[2] C. P. Singh,[2] V. Singh,[2] M. Slunečka,[7] R. A. Soltz,[35] W. E. Sondheim,[36] S. P. Sorensen,[59] I. V. Sourikova,[5] N. A. Sparks,[1] P. W. Stankus,[47] E. Stenlund,[38] S. P. Stoll,[5] T. Sugitate,[21] A. Sukhanov,[5] J. Sziklai,[30] E. M. Takagui,[55] A. Taketani,[51,52] R. Tanabe,[61] Y. Tanaka,[44] K. Tanida,[33,51,52] M. J. Tannenbaum,[5] S. Tarafdar,[2] A. Taranenko,[57] P. Tarján,[15] H. Themann,[58] T. L. Thomas,[45] M. Togawa,[33,51] A. Toia,[58] L. Tomášek,[25] H. Torii,[21] R. S. Towell,[1] I. Tserruya,[64] Y. Tsuchimoto,[21] C. Vale,[5,26] H. Valle,[62] H. W. van Hecke,[36] E. Vazquez-Zambrano,[12] A. Veicht,[23] J. Velkovska,[62] R. Vértesi,[15,30] A. A. Vinogradov,[32] M. Virius,[13] V. Vrba,[25] E. Vznuzdaev,[50] X. R. Wang,[46] D. Watanabe,[21] K. Watanabe,[61] Y. Watanabe,[51,52] F. Wei,[26] R. Wei,[57] J. Wessels,[41] S. N. White,[5] D. Winter,[12] J. P. Wood,[1] C. L. Woody,[5] R. M. Wright,[1] M. Wysocki,[11] W. Xie,[52] Y. L. Yamaguchi,[10] K. Yamaura,[21] R. Yang,[23] A. Yanovich,[22] J. Ying,[20] S. Yokkaichi,[51,52] G. R. Young,[47] I. Younus,[45] Z. You,[49] I. E. Yushmanov,[32] W. A. Zajc,[12] C. Zhang,[47] S. Zhou,[9] and L. Zolin[27]

(PHENIX Collaboration)

[1]*Abilene Christian University, Abilene, Texas 79699, USA*

[2]*Department of Physics, Banaras Hindu University, Varanasi 221005, India*

[3]*Bhabha Atomic Research Centre, Bombay 400 085, India*

[4]*Collider-Accelerator Department, Brookhaven National Laboratory, Upton, New York 11973-5000, USA*

[5]*Physics Department, Brookhaven National Laboratory, Upton, New York 11973-5000, USA*

[6]*University of California Riverside, Riverside, California 92521, USA*

[7]*Charles University, Ovocný trh 5, Praha 1, CZ-116 36 Prague, Czech Republic*

[8]*Chonbuk National University, Jeonju 561-756, Korea*

[9]*China Institute of Atomic Energy (CIAE), Beijing 102413, P. R. China*

[10]*Center for Nuclear Study, Graduate School of Science, University of Tokyo, 7-3-1 Hongo, Bunkyo, Tokyo 113-0033, Japan*
[11]*University of Colorado, Boulder, Colorado 80309, USA*
[12]*Columbia University, New York, New York 10027, and Nevis Laboratories, Irvington, New York 10533, USA*
[13]*Czech Technical University, Zikova 4, CZ-166 36 Prague 6, Czech Republic*
[14]*Dapnia, CEA Saclay, F-91191 Gif-sur-Yvette, France*
[15]*Debrecen University, Egyetem tér 1, H-4010 Debrecen, Hungary*
[16]*ELTE, Eötvös Loránd University, Pázmány P. s. 1/A, H-1117 Budapest, Hungary*
[17]*Ewha Womans University, Seoul 120-750, Korea*
[18]*Florida Institute of Technology, Melbourne, Florida 32901, USA*
[19]*Florida State University, Tallahassee, Florida 32306, USA*
[20]*Georgia State University, Atlanta, Georgia 30303, USA*
[21]*Hiroshima University, Kagamiyama, Higashi-Hiroshima 739-8526, Japan*
[22]*IHEP Protvino, State Research Center of Russian Federation, Institute for High Energy Physics, Protvino 142281, Russia*
[23]*University of Illinois at Urbana-Champaign, Urbana, Illinois 61801, USA*
[24]*Institute for Nuclear Research of the Russian Academy of Sciences, prospekt 60-letiya Oktyabrya 7a, Moscow 117312, Russia*
[25]*Institute of Physics, Academy of Sciences of the Czech Republic, Na Slovance 2, CZ-182 21 Prague 8, Czech Republic*
[26]*Iowa State University, Ames, Iowa 50011, USA*
[27]*Joint Institute for Nuclear Research, 141980 Dubna, Moscow Region, Russia*
[28]*Helsinki Institute of Physics and University of Jyväskylä, P.O. Box 35, FI-40014 Jyväskylä, Finland*
[29]*KEK, High Energy Accelerator Research Organization, Tsukuba, Ibaraki 305-0801, Japan*
[30]*KFKI Research Institute for Particle and Nuclear Physics of the Hungarian Academy of Sciences (MTA KFKI RMKI), P.O. Box 49, H-1525 Budapest 114, Hungary*
[31]*Korea University, Seoul 136-701, Korea*
[32]*Russian Research Center "Kurchatov Institute," Moscow 123098, Russia*
[33]*Kyoto University, Kyoto 606-8502, Japan*
[34]*Laboratoire Leprince-Ringuet, Ecole Polytechnique, CNRS-IN2P3, Route de Saclay, F-91128 Palaiseau, France*
[35]*Lawrence Livermore National Laboratory, Livermore, California 94550, USA*
[36]*Los Alamos National Laboratory, Los Alamos, New Mexico 87545, USA*
[37]*LPC, Université Blaise Pascal, CNRS-IN2P3, Clermont-Fd, F-63177 Aubiere Cedex, France*
[38]*Department of Physics, Lund University, Box 118, SE-221 00 Lund, Sweden*
[39]*University of Maryland, College Park, Maryland 20742, USA*
[40]*Department of Physics, University of Massachusetts, Amherst, Massachusetts 01003-9337, USA*
[41]*Institut fur Kernphysik, University of Muenster, D-48149 Muenster, Germany*
[42]*Muhlenberg College, Allentown, Pennsylvania 18104-5586, USA*
[43]*Myongji University, Yongin, Kyonggido 449-728, Korea*
[44]*Nagasaki Institute of Applied Science, Nagasaki-shi, Nagasaki 851-0193, Japan*
[45]*University of New Mexico, Albuquerque, New Mexico 87131, USA*
[46]*New Mexico State University, Las Cruces, New Mexico 88003, USA*
[47]*Oak Ridge National Laboratory, Oak Ridge, Tennessee 37831, USA*
[48]*IPN-Orsay, Universite Paris Sud, CNRS-IN2P3, BP1, F-91406 Orsay, France*
[49]*Peking University, Beijing 100871, P. R. China*
[50]*PNPI, Petersburg Nuclear Physics Institute, Gatchina, 188300 Leningrad region, Russia*
[51]*RIKEN Nishina Center for Accelerator-Based Science, Wako, Saitama 351-0198, Japan*
[52]*RIKEN BNL Research Center, Brookhaven National Laboratory, Upton, New York 11973-5000, USA*
[53]*Physics Department, Rikkyo University, 3-34-1 Nishi-Ikebukuro, Toshima, Tokyo 171-8501, Japan*
[54]*Saint Petersburg State Polytechnic University, 195251 St. Petersburg, Russia*
[55]*Universidade de São Paulo, Instituto de Física, Caixa Postal 66318, São Paulo CEP05315-970, Brazil*
[56]*Seoul National University, Seoul, Korea*
[57]*Chemistry Department, Stony Brook University, SUNY, Stony Brook, New York 11794-3400, USA*
[58]*Department of Physics and Astronomy, Stony Brook University, SUNY, Stony Brook, New York 11794-3400, USA*
[59]*University of Tennessee, Knoxville, Tennessee 37996, USA*
[60]*Department of Physics, Tokyo Institute of Technology, Oh-okayama, Meguro, Tokyo 152-8551, Japan*
[61]*Institute of Physics, University of Tsukuba, Tsukuba, Ibaraki 305, Japan*
[62]*Vanderbilt University, Nashville, Tennessee 37235, USA*
[63]*Waseda University, Advanced Research Institute for Science and Engineering, 17 Kikui-cho, Shinjuku-ku, Tokyo 162-0044, Japan*
[64]*Weizmann Institute, Rehovot 76100, Israel*
[65]*Yonsei University, IPAP, Seoul 120-749, Korea*
(Received 31 March 2011; published 21 November 2011)

Heavy quarkonia are observed to be suppressed in relativistic heavy-ion collisions relative to their production in $p + p$ collisions scaled by the number of binary collisions. In order to determine if this suppression is related to color screening of these states in the produced medium, one needs to account for other nuclear modifications including those in cold nuclear matter. In this paper, we present new measurements from the PHENIX 2007 data set of J/ψ yields at forward rapidity ($1.2 < |y| < 2.2$) in Au + Au collisions at $\sqrt{s_{NN}} = 200$ GeV. The data confirm the earlier finding that the suppression of J/ψ at forward rapidity is stronger than at midrapidity, while also extending the measurement to finer bins in collision centrality and higher transverse momentum (p_T). We compare the experimental data to the most recent theoretical calculations that incorporate a variety of physics mechanisms including gluon saturation, gluon shadowing, initial-state parton energy loss, cold nuclear matter breakup, color screening, and charm recombination. We find J/ψ suppression beyond cold-nuclear-matter effects. However, the current level of disagreement between models and d + Au data precludes using these models to quantify the hot-nuclear-matter suppression.

DOI: 10.1103/PhysRevC.84.054912 PACS number(s): 25.75.Dw

I. INTRODUCTION

Heavy quarkonia have long been proposed as a sensitive probe of the color screening length and deconfinement in the quark-gluon plasma [1]. The picture that was originally proposed is complicated by other competing effects that modify quarkonia production and survival in cold and hot nuclear matter. The large suppression of J/ψ in Pb + Pb collisions at $\sqrt{s_{NN}} = 17.2$ GeV measured by the NA50 experiment indicated suppression beyond that projected from cold-nuclear-matter effects and led to the initial conclusion that color screening was the dominant mechanism [2–4]. The expectation was that at the Relativistic Heavy Ion Collider (RHIC), where higher energy densities and temperatures are created, the J/ψ suppression would be stronger and turn on in even more peripheral collisions. However, measurements from the PHENIX experiment's 2004 data set in Au + Au collisions at $\sqrt{s_{NN}} = 200$ GeV revealed that the centrality-dependent nuclear modification factor R_{AA} at midrapidity was the same within statistical and systematic uncertainties as the NA50 result [5–7]. In addition, for central collisions ($N_{\rm part} \gtrsim 100$) the suppression was measured to be larger at forward rapidity ($1.2 < |y| < 2.2$) compared with midrapidity [5]. This is opposite to the expectation that the suppression should be less at forward rapidity, where the energy density is lower.

The initial estimates of cold-nuclear-matter (CNM) effects in the NA50 Pb + Pb data were based on $p + A$ measurements [8] at higher collision energies. More recently, measurements of J/ψ production in $p + A$ collisions at $\sqrt{s_{NN}} = 17.2$ GeV made by NA60 have shown that CNM effects are stronger than the initial estimates, due to a substantially larger J/ψ effective breakup cross section [9]. This resulted in a reduction of the estimated suppression due to possible hot-nuclear-matter effects from ∼50% to ∼25%, relative to cold-nuclear-matter effects. Based on a systematic study of the energy dependence [10] the breakup cross section is expected to be much smaller at the higher RHIC energies, leading to smaller overall CNM effects. Thus it now seems that at RHIC the suppression beyond CNM effects at midrapidity could be higher than the suppression observed in the NA50 results, as one would expect due to the higher energy density. However, why the observed suppression at RHIC is stronger at forward rapidity than at midrapidity remains a question.

Since that first PHENIX measurement, many alternative explanations have been proposed which require rigorous confrontation with the full set of experimental measurements. In this paper, we detail the measurement of forward rapidity J/ψ yields and modifications in Au + Au collisions at $\sqrt{s_{NN}} =$ 200 GeV from data taken by the PHENIX experiment in 2007. The data set is more than three times larger than the earlier published 2004 data set. In addition, significant improvements in our understanding of the detector performance and signal extraction have led to a reduction in systematic uncertainties. We present details of this analysis as well as comparisons with theoretical calculations that have been used in attempts to explain the earlier data in terms of competing mechanisms.

II. DATA ANALYSIS

The PHENIX experiment is described in detail in [11]. For the forward rapidity J/ψ data analysis presented here, the PHENIX experiment utilizes one global detector, the beam-beam counter (BBC), for event centrality characterization and z-vertex determination, and two muon spectrometers (north and south) for measuring J/ψ yields via the dimuon decay channel. The BBC is described in detail in [12]. It comprises two arrays of 64 quartz Čerenkov counters that detect charged particles within the pseudorapidity range $3.0 < |\eta| < 3.9$. The BBC is also used as the primary level-1 trigger for Au + Au minimum-bias events. The two muon spectrometers, described in detail in [13], comprise an initial hadronic absorber followed by three sets of cathode strip chambers in a magnetic field, referred to as the muon tracker (MuTr). Finally, there are five planes of active Iarocci tubes interleaved with additional steel absorber plates, referred to as the muon identifier (MuID). The muon spectrometers measure J/ψ yields over the rapidity range $1.2 < |y| < 2.2$.

The PHENIX data-acquisition system is capable of recording minimum-bias Au + Au collisions at high rates (> 5 kHz) with a data archival rate in excess of 600 MB/s. During the 2007 Au + Au run at $\sqrt{s_{NN}} = 200$ GeV, the experiment recorded 82% of all collisions where the minimum bias level-1 trigger fired. Therefore no additional muon-specific trigger

*Deceased.
†PHENIX Spokesperson: jacak@skipper.physics.sunysb.edu

was necessary. After making data quality cuts to remove runs where there were significant detector performance variations, we analyzed 3.6×10^9 minimum-bias Au + Au events. The BBC level-1 trigger used as the minimum-bias trigger for Au + Au events required at least two hits in each of the BBC arrays and a fast-reconstructed z vertex within ± 30 cm of the nominal center of the detector. An additional selection for our minimum-bias definition in offline reconstruction includes a requirement of at least one neutron hit in each of our zero-degree calorimeters. This removes a 1%–2% background event contamination in the peripheral event sample. The minimum-bias definition corresponds to $92\% \pm 3\%$ of the inelastic Au + Au cross section [5]. We further categorize the events in terms of centrality classes by comparing the combined north and south BBC charge to a negative binomial distribution for the number of produced particles within the BBC acceptance combined with a Glauber model of the collision [14]. For each centrality category, the mean number of participating nucleons ($N_{\rm part}$), the mean number of binary collisions ($N_{\rm coll}$), the impact parameter (b), and their associated systematic uncertainties are shown in Table I.

From this minimum-bias data sample, we reconstruct muon candidates by finding tracks that penetrate through all layers of the MuID, then matching to tracks in the MuTr. The requirement of the track penetrating the full absorber material through the MuID significantly reduces the hadron contribution. However, there is a small probability of order $\sim 1/1000$ for a charged hadron to penetrate the material without suffering a hadronic interaction. This is referred to as a punch-through hadron. Additionally, the current muon spectrometer cannot reject most muons that originate from charged pions and kaons which decay before the absorber in front of the MuTr. Pairs of muon candidate tracks are selected and a combined fit is performed with the collision z vertex from the BBC. We apply various cuts to enhance the signal-to-background ratio for the muon track pairs, including cuts on the individual track χ^2 values, the matching between position and direction vectors of the MuID track and the MuTr track projected to the front of the MuID, and finally the track pair and BBC z-vertex combined fit $\chi^2_{\rm vtx}$.

TABLE I. Mean $N_{\rm part}$, mean $N_{\rm coll}$, impact parameter values, and systematic uncertainties in each centrality category.

Centrality (%)	$\langle N_{\rm part} \rangle$	$\langle N_{\rm coll} \rangle$	$\langle b \rangle$ (fm)
0–5	350.8 ± 3.1	1067.0 ± 107.7	2.3 ± 0.1
5–10	301.7 ± 4.7	857.8 ± 85.5	3.9 ± 0.1
10–15	255.7 ± 5.4	680.2 ± 67.3	5.2 ± 0.2
15–20	216.4 ± 5.6	538.7 ± 52.4	6.1 ± 0.2
20–25	182.4 ± 5.7	424.4 ± 40.4	7.0 ± 0.3
25–30	152.7 ± 5.9	330.9 ± 32.7	7.7 ± 0.3
30–35	126.8 ± 5.9	254.7 ± 25.8	8.4 ± 0.3
35–40	104.2 ± 5.8	193.1 ± 20.7	9.0 ± 0.3
40–45	84.6 ± 5.6	143.9 ± 16.5	9.6 ± 0.4
45–50	67.7 ± 5.4	105.4 ± 13.5	10.2 ± 0.4
50–55	53.2 ± 5.0	75.2 ± 10.5	10.7 ± 0.4
55–60	41.0 ± 4.5	52.5 ± 8.2	11.2 ± 0.4
60–65	30.8 ± 3.9	35.7 ± 6.1	11.7 ± 0.5
65–70	22.6 ± 3.4	23.8 ± 4.7	12.2 ± 0.5
70–75	16.1 ± 2.8	15.4 ± 3.3	12.6 ± 0.5
75–80	11.2 ± 2.2	9.7 ± 2.3	13.1 ± 0.5
80–92	5.6 ± 0.8	4.2 ± 0.8	13.9 ± 0.5
0–20	280.5 ± 4.6	783.2 ± 77.5	4.4 ± 0.2
20–40	141.5 ± 5.8	300.8 ± 29.6	8.0 ± 0.3
40–60	61.6 ± 5.1	94.2 ± 12.0	10.4 ± 0.4
60–92	14.4 ± 2.1	14.5 ± 2.8	13.0 ± 0.5

We then calculate the invariant mass of all muon candidate unlike-charged-sign pairs in various bins in rapidity, p_T, and centrality. Due to the high particle multiplicity in Au + Au events, there is a significant background under the J/ψ peak. In the 0%–5% most central Au + Au collisions, within the mass window around the J/ψ ($2.6 < M$ [GeV/c^2] < 3.6) the signal to background is of order 2.9% in the south muon spectrometer and 0.7% in the north muon spectrometer (which has a different geometric acceptance and significantly higher occupancy). The background comprises two components. First, there is the combinatorial background from uncorrelated track pairs. Second, there is a correlated background from physical sources including semileptonic decays of open charm pairs [e.g., $D^0 + \overline{D^0} \to (K^- \mu^+ \nu_\mu) + (K^+ \mu^- \overline{\nu_\mu})$, open beauty pair decays, and Drell-Yan]. The combinatorial background is estimated and subtracted by using event mixing to recreate the background from uncorrelated pairs. In this procedure, pairs are created from different Au + Au events within the same category in Au + Au centrality and BBC collision z vertex. The mixed-event invariant-mass distributions are calculated for unlike-sign and like-sign pairs. We treat the real-event like-sign pairs as being purely from combinatorial background, since the contribution of the above-mentioned correlated physical background is negligible relative to the combinatorial background. Thus, we determine the mixed-event normalization for the unlike-sign case by calculating the normalization factor between the mixed-event and real-event like-sign counts. We have confirmed that the mixed-event and real-event like-sign invariant-mass distributions match over the full mass range used in the analysis.

The total J/ψ counts recorded in all Au + Au collisions are $\sim$9100 and $\sim$4900 in the south and north muon spectrometers, respectively. Figure 1 shows two examples of unlike-sign invariant-mass distributions before (upper panels) and after (lower panels) mixed-event combinatorial background subtraction. The measured J/ψ yield is derived from the subtracted spectrum by fitting to the data the line shape of the J/ψ, as determined in $p + p$ collisions [15], and an exponential for the remaining correlated physical background. Note that in the p_T bins above 2 GeV/c, there is some small acceptance for the ρ, ω, and ϕ and thus these additional components are included in the fit. At low p_T, the acceptance goes to zero for low invariant masses due to the required minimum momentum for each muon to penetrate the MuID and the angular acceptance of the spectrometer. This is accounted for by folding the fit function with an acceptance function that is calculated from Monte Carlo simulation and which goes to zero at small invariant mass, as expected. We perform a set of fits where we vary the invariant-mass range, the line shape of the J/ψ, and the normalization of the mixed-event

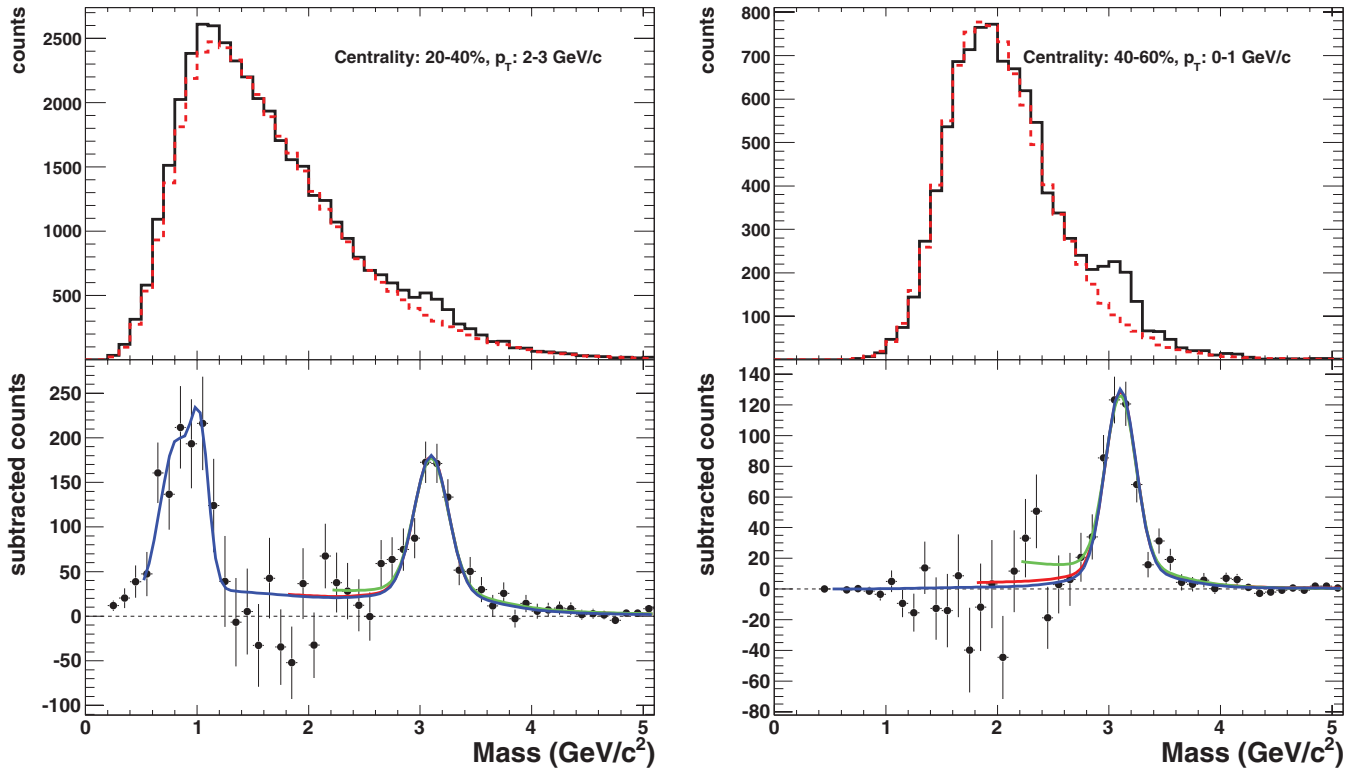

FIG. 1. (Color online) For the two indicated centrality bins and transverse momentum ranges (top panels) muon spectrometer unlike-sign invariant-mass distributions from same-event pairs (black, solid) and mixed-event pairs (red, dashed) and (bottom panels) corresponding unlike-sign invariant-mass distributions after mixed-event combinatorial-background subtraction. The curves in the bottom panels are fits resulting from using three different mass ranges for the signal extraction.

sample by $\pm 2\%$ to determine the mean extracted J/ψ signal and systematic uncertainty from the rms values of the different results. Note that any bin where the extracted signal is of less than one standard deviation significance (including statistical and systematic uncertainties) is quoted as a 90% confidence level upper limit (CLUL) based on Poisson statistics.

We also estimated the combinatorial background using the like-sign method, i.e., $N_{+-}^{\rm comb} = 2\sqrt{N_{++} \times N_{--}}$. In this case there is no event mixing, and the background is estimated purely from same-event like-sign pairs (instead of mixed-event pairs). The two methods agree over most of the centrality range; however, for the more central events the like-sign method results in somewhat lower extracted counts ($\sim 10\%$). We take the average of the two signal extraction methods and assign an additional systematic uncertainty due to the difference, although for peripheral bins it is a negligible difference.

We then calculate the J/ψ invariant yield for each centrality bin and also in bins in p_T by the following equation:

$$\frac{B_{\mu\mu}}{2\pi\, p_T}\frac{d^2N}{d\,p_T dy} = \frac{1}{2\pi\, p_T \Delta p_T \Delta y}\frac{N_{J/\psi}}{A\epsilon N_{EVT}}, \qquad (1)$$

where $B_{\mu\mu}$ is the branching fraction of J/ψ to muons, $N_{J/\psi}$ is the measured J/ψ yield, N_{EVT} is the number of events in the relevant Au + Au centrality category, $A\epsilon$ is the detector geometric acceptance times efficiency, and Δp_T and Δy are the bin widths in p_T and y. For the p_T-integrated bins, we similarly calculate $B_{\mu\mu} dN/dy = N_{J/\psi}/(A\epsilon N_{EVT} \Delta y)$.

We calculate $A\epsilon$ to correct for the geometric acceptance of the detector and the inefficiencies of the MuTr and MuID, the track finding algorithm, and occupancy-related effects in the Au + Au environment. This is done by propagating PYTHIA-generated J/ψ through the PHENIX GEANT-3 [16] detector simulation and embedding the resulting hits into real events. The events are then reconstructed using the identical analysis as for real data, and the ratio is taken between reconstructed and embedded J/ψ. The resulting $A\epsilon$ as a function of centrality is shown in Fig. 2 for both the north and south muon arms. The effect of the detector occupancy can be seen for more central events, as well as the higher occupancy and resulting lower efficiency in the north arm.

Only statistical uncertainties from the detector simulation are shown. In addition, a systematic uncertainty arises from determination of the reconstruction efficiency in central events. When the centrality-dependent efficiencies are plotted as a function of detector occupancy, both muon arms follow the same efficiency curve. Consequently, any differences in the final invariant yields between the two arms provide a good check of the efficiency calculation. These differences are small and are accounted for in the systematic uncertainties. We also compare the above embedding study with one where "golden" real-data J/ψs from $p + p$ events are embedded into Au + Au underlying events and the relative efficiency as

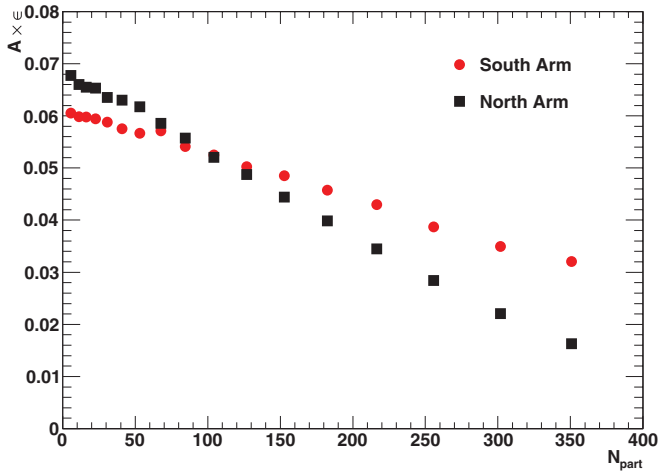

FIG. 2. (Color online) Acceptance times efficiency as a function of centrality for the north and south arms.

a function of centrality is again reflected in the systematic uncertainties.

The acceptance and efficiency as a function of p_T is relatively flat, with a modest 20% decrease from p_T = 0 to $p_T \sim 2.5$ GeV/c^2, followed by a rise. The behavior is essentially the same across centralities, with the only difference being the absolute scale of $A\epsilon$.

We calculate the invariant yields separately from the two muon spectrometers, and then combine the values for the final results. We take the weighted average based on the statistical uncertainties and those systematic uncertainties which are uncorrelated between the two measurements. The final averaged result is assigned the uncorrelated (reduced by the averaging) and correlated systematic uncertainties. In addition, it was found that the invariant yields from the two spectrometers disagree beyond their independent uncertainties, and a 5% systematic was added to account for the difference.

III. RESULTS

The final J/ψ invariant yields in 5%-wide centrality bins (integrated over all p_T) are listed in Table II, and those as a function of p_T in broader 20%-wide centrality bins are listed in Table III.

The nuclear modification factor $R_{\rm AA}$ compares J/ψ production in $A + A$ with binary-collision-scaled $p + p$ reactions and is calculated as

$$R_{\rm AA} = \frac{1}{\langle N_{\rm coll}\rangle} \frac{dN^{A+A}/dy}{dN^{p+p}/dy}, \tag{2}$$

where $\langle N_{\rm coll}\rangle$ is the mean number of binary collisions in the centrality category of interest. The $p + p$ results are from the combined analysis of data taken in 2006 and 2008 as published in [17]. The resulting forward rapidity $R_{\rm AA}$ as a function of $N_{\rm part}$ for J/ψ from Au + Au collisions is shown as red circles in Fig. 3.

The systematic uncertainties are divided into three categories: type A are the point-to-point uncorrelated systematics, type B are point-to-point correlated (or anticorrelated), and type C are 100% correlated (i.e., share a common multiplicative factor) among all of the points. The error bars in Figs. 3–10 represent the statistical and type A uncertainties added in quadrature, the boxes represent the type B uncertainties, while the type C systematics are included as text in the labels. The type A uncertainties are the rms values of the various mass fits as described above. The type B uncertainties on $R_{\rm AA}$ are dominated by uncertainties in $N_{\rm coll}$, uncertainties in the

TABLE II. J/ψ invariant yields $B_{\mu\mu}dN/dy$ at forward rapidity ($1.2 < |y| < 2.2$) vs Au + Au collision centrality. The statistical uncertainties, the type A systematic uncertainties (point-to-point uncorrelated), and the type B systematic uncertainties (point-to-point correlated) are shown. The type C (global) uncertainty for all points is 10.7%.

Centrality (%)	$B_{\mu\mu}dN/dy$	± Statistical	± Type A	+Type B	−Type B	Scale factor
0–5	1.25	0.27	0.11	0.24	0.12	$\times 10^{-4}$
5–10	9.12	2.46	0.13	1.15	0.81	$\times 10^{-5}$
10–15	9.37	1.66	0.71	1.01	0.95	$\times 10^{-5}$
15–20	9.16	1.24	0.48	1.08	1.08	$\times 10^{-5}$
20–25	7.11	0.98	0.29	0.64	0.64	$\times 10^{-5}$
25–30	7.85	0.74	0.29	0.64	0.64	$\times 10^{-5}$
30–35	6.14	0.57	0.28	0.49	0.49	$\times 10^{-5}$
35–40	5.43	0.45	0.14	0.52	0.52	$\times 10^{-5}$
40–45	5.07	0.37	0.15	0.39	0.39	$\times 10^{-5}$
45–50	3.49	0.28	0.07	0.30	0.30	$\times 10^{-5}$
50–55	2.76	0.21	0.07	0.21	0.21	$\times 10^{-5}$
55–60	2.85	0.17	0.04	0.21	0.21	$\times 10^{-5}$
60–65	1.64	0.14	0.03	0.12	0.12	$\times 10^{-5}$
65–70	1.17	0.10	0.01	0.09	0.09	$\times 10^{-5}$
70–75	9.49	0.85	0.11	0.73	0.73	$\times 10^{-6}$
75–80	6.79	0.69	0.14	0.51	0.51	$\times 10^{-6}$
80–92	3.43	0.29	0.04	0.26	0.26	$\times 10^{-6}$

TABLE III. J/ψ invariant yields $B_{\mu\mu}\frac{d^3N}{dp_T{}^2dy}$ at forward rapidity ($1.2 < |y| < 2.2$) vs p_T in four bins of Au + Au collision centrality. The statistical uncertainties, the type A systematic uncertainties (point-to-point uncorrelated), and the type B systematic uncertainties (point-to-point correlated) are shown. The type C (global) uncertainties are 10%, 10%, 13%, and 19% for 0%–20%, 20%–40%, 40%–60%, and 60%–92% centrality, respectively. Bins in which the J/ψ yield was less than the combined statistical and systematic uncertainties are calculated as 90% confidence level upper limits (CLUL).

Centrality (%)	p_T (GeV/c)	$B_{\mu\mu}\frac{d^3N}{dp_T{}^2dy}$	Statistical	Type A	Type B	Scale factor
			$(\mathrm{Gev}/c)^{-2}$			
0–20	0–1	9.36	1.41	0.74	1.01	$\times 10^{-6}$
	1–2	4.46	0.66	0.23	0.40	$\times 10^{-6}$
	2–3	1.37	0.29	0.08	0.17	$\times 10^{-6}$
	3–4	2.99	1.12	0.09	0.27	$\times 10^{-7}$
	4–5	2.05	0.43	0.14	0.18	$\times 10^{-7}$
	5–6		90% CLUL = 3.27			$\times 10^{-8}$
	6–7		90% CLUL = 2.00			$\times 10^{-8}$
20–40	0–1	5.08	0.54	0.18	0.67	$\times 10^{-6}$
	1–2	2.78	0.22	0.09	0.26	$\times 10^{-6}$
	2–3	1.11	0.10	0.02	0.09	$\times 10^{-6}$
	3–4	2.76	0.34	0.11	0.25	$\times 10^{-7}$
	4–5	7.47	1.37	0.31	1.35	$\times 10^{-8}$
	5–6	2.68	0.61	0.08	0.31	$\times 10^{-8}$
	6–7		90% CLUL = 7.15			$\times 10^{-9}$
40–60	0–1	3.19	0.21	0.06	0.26	$\times 10^{-6}$
	1–2	1.49	0.09	0.03	0.12	$\times 10^{-6}$
	2–3	4.80	0.38	0.11	0.39	$\times 10^{-7}$
	3–4	1.27	0.13	0.02	0.11	$\times 10^{-7}$
	4–5	3.86	0.49	0.02	0.41	$\times 10^{-8}$
	5–6	7.51	1.69	0.05	2.04	$\times 10^{-9}$
	6–7		90% CLUL = 2.82			$\times 10^{-9}$
60–92	0–1	9.05	0.57	0.07	0.73	$\times 10^{-7}$
	1–2	3.40	0.22	0.04	0.27	$\times 10^{-7}$
	2–3	9.19	0.91	0.16	0.75	$\times 10^{-8}$
	3–4	2.21	0.35	0.04	0.20	$\times 10^{-8}$
	4–5	8.13	1.39	0.01	0.70	$\times 10^{-9}$
	5–6	2.31	0.54	0.00	0.40	$\times 10^{-9}$
	6–7		90% CLUL = 7.69			$\times 10^{-10}$

matching of Monte Carlo and real detector performance, differences in signal extraction methods, and determination of the occupancy-dependent efficiency in central Au + Au events. The type C uncertainties are dominated by the normalization in the $p + p$-invariant cross section measurement. Important systematics on the invariant yields are listed in Table IV.

For comparison, in Fig. 3 we show as blue squares our previously published midrapidity J/ψ R_{AA} values from data taken in 2004 [5]. The midrapidity measurement was made in the PHENIX central spectrometers via the J/ψ dielectron decay. There is no PHENIX updated measurement at midrapidity from the 2007 data set due to significantly increased conversion backgrounds from this engineering run of the PHENIX Hadron Blind Detector [18]. The ratio of the new forward rapidity data to the previously published midrapidity data, shown in the lower panel of Fig. 3, is in agreement with the previous result [5], where the latter led to speculation as to

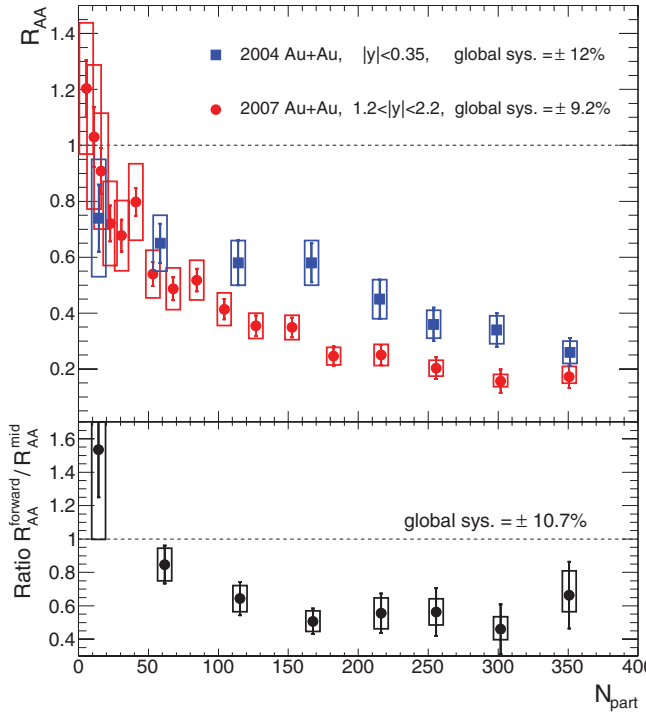

FIG. 3. (Color online) Measured J/ψ nuclear modification factors R_{AA} vs N_{part}. The lower panel shows the ratio of forward rapidity (circles, red) to midrapidity (squares, blue) for the points in the upper panel. The error bars represent the statistical and uncorrelated systematic uncertainties, while the boxes represent the point-to-point correlated systematics. The global scale systematic uncertainties are indicated.

what mechanism could cause a narrower rapidity distribution in Au + Au collisions than in $p + p$ collisions.

We also calculate R_{AA} as a function of p_T, again using the published 2006 and 2008 $p + p$ data [17]. Shown in Fig. 4 are the new results at forward rapidity along with the previously published 2004 midrapidity results [5]. In some centrality bins for $p_T > 5$ GeV/c, we have no significant J/ψ signal in Au + Au and thus can only quote a 90% confidence level upper limit on R_{AA}.

As there has been much recent interest in whether R_{AA} as a function of p_T rises or falls, we have performed a simple linear fit to R_{AA} at forward rapidity over the full p_T range and obtain the following slope (m) values: $m = +0.011 \pm 0.018c/\mathrm{GeV}$ (0%–20% central), $m = +0.065 \pm 0.023c/\mathrm{GeV}$ (20%–40% central), $m = +0.034 \pm 0.033c/\mathrm{GeV}$ (40%–60% central), and $m = -0.037 \pm 0.053c/\mathrm{GeV}$ (60%–92% central). The quoted slope uncertainties are the quadrature sum of the statistical and systematic uncertainties. Thus, only for the 20%–40% centrality bin is there a statistically significant increase in R_{AA} with p_T.

IV. MODEL COMPARISONS

As previously mentioned, various theoretical models have been proposed to explain the J/ψ suppression pattern previously published [5]. Here we compare our measurements

TABLE IV. Systematic uncertainties on dN/dy for central and peripheral centrality categories.

Source	Central	Peripheral	Type
Signal extraction	9.8%	1.3%	A
Acceptance	3.4%	2.2%	B
Occupancy efficiency	16.0%	0.0%	B
Input y, p_T distributions	4%	4%	B
Difference between mixed event and like-sign background estimates	1.5%	0.6%	B
North-south arm agreement	5%	5%	B
MuID efficiency	3.6%	2.8%	B

with three calculations for the centrality and rapidity dependence of the suppression. The first deals entirely with initial-state effects, while the other two incorporate strong final-state effects. Then we compare our measurements with a simple cold-nuclear-matter-effect calculation extrapolated to Au + Au collisions. Finally, we compare to a model calculation for the p_T dependence of $R_{\rm AA}$ at forward rapidity.

In addition to the models discussed here, there are many more models that only have a midrapidity prediction for J/ψ production. Because this paper is focused on forward rapidity J/ψ production, we have not included comparisons to those models.

A. Gluon saturation

In the first model, by Kharzeev *et al.* [19], it is assumed that the nuclear wave functions in very high energy nuclear collisions can be described by the color glass condensate (CGC). The primary effect is the suppression of J/ψ production and narrowing of the rapidity distribution due to saturation of the gluon fields in heavy-ion collisions relative to $p + p$ collisions. In addition, the production mechanism is modified from $p + p$ such that the multigluon exchange diagrams are enhanced. It should be noted that this model does not include any hot-medium effects, but it does have a free parameter for the overall normalization factor for the Au + Au production, which is fixed to match the midrapidity central collision J/ψ suppression. Thus, the suppression trend with centrality and the relative suppression between midrapidity and forward rapidity are predicted, but not the overall level of suppression.

The resulting $R_{\rm AA}$ values calculated using this model are shown in Fig. 5. This model provides a reasonable description of the data and in particular better matches the observed larger suppression at forward rapidity than at midrapidity in central events ($R_{\rm AA}^{\rm forward}/R_{\rm AA}^{\rm mid} \sim 0.5$). It is notable that this ratio is essentially independent of centrality in their calculation, whereas the experimental data show the relative suppression approaching one in the most peripheral events. Additionally, the calculation at midrapidity actually indicates a significant enhancement (i.e., $R_{\rm AA} > 1$) for peripheral events with $N_{\rm part} < 50$. This enhancement is related to a coherence effect of double gluon exchange. However, the coherence predicts an enhancement in d + Au collisions and $R_{d\rm Au}$ at midrapidity, and no such enhancement is seen in the experimental data [17].

Recently, the appropriate normalization factor for the above CGC calculation has been calculated [20,21]. Replacing the normalization factor previously applied to match the theory to the magnitude of the observed midrapidity suppression results in a predicted CGC suppression that is approximately a factor

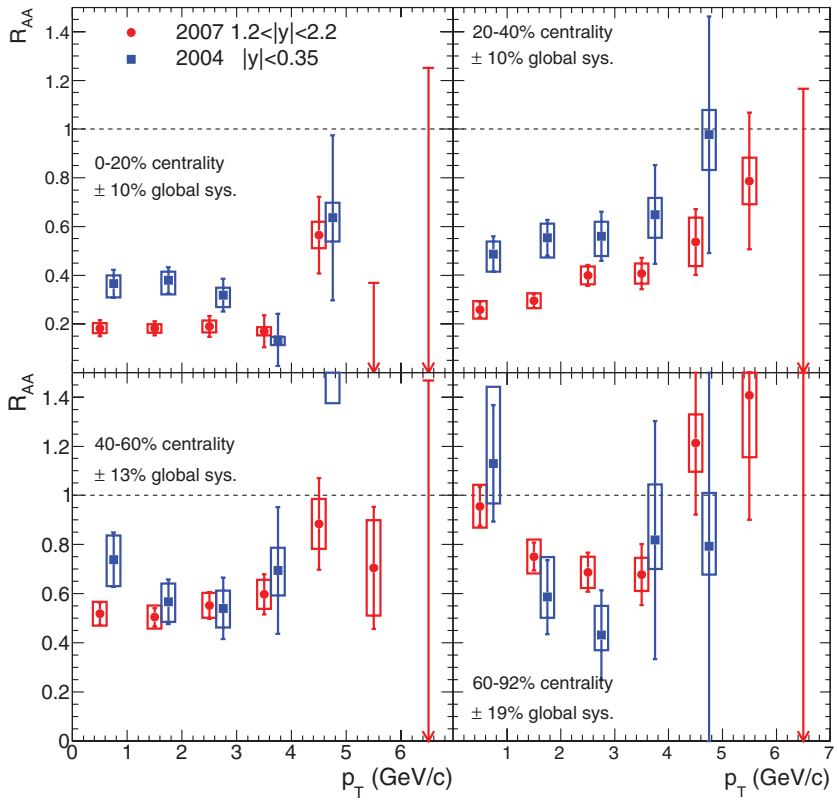

FIG. 4. (Color online) Measured J/ψ $R_{\rm AA}$ vs p_T for the four indicated centrality bins. The error bars represent the statistical and uncorrelated systematic uncertainties, while the boxes represent the point-to-point correlated systematic uncertainties. The global scale systematic uncertainties are indicated.

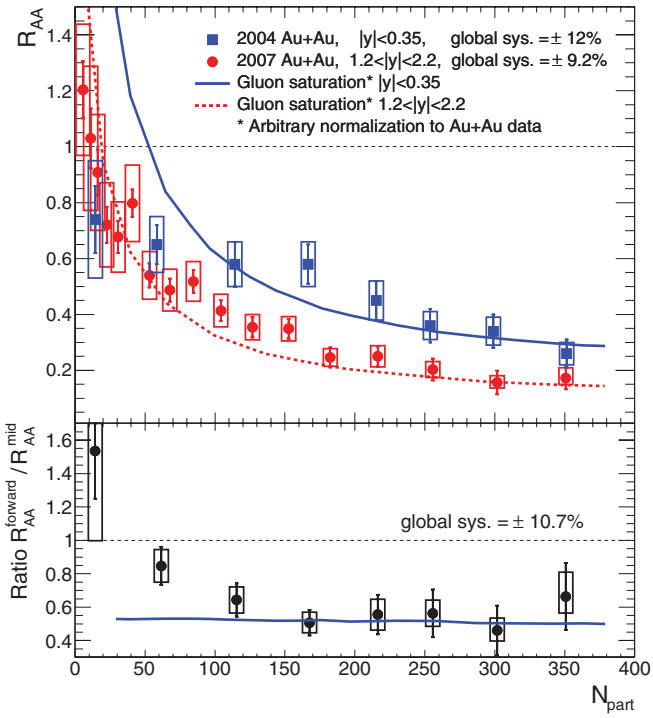

FIG. 5. (Color online) Measured J/ψ R_{AA} vs N_{part} from Fig. 3 and gluon saturation calculations [19]. The lower panel shows ratios of forward to midrapidity points and curves from the upper panel. The round (red) data points and dashed (red) curves are for forward rapidity ($1.2 < |y| < 2.2$), while the square (blue) data points and solid (blue) curves are for midrapidity ($|y| < 0.35$).

of 2 smaller than in the Au + Au data. This result suggests the importance of additional hot-nuclear-matter effects.

B. Comover interaction

The second calculation comes from the comover interaction model (CIM) [22,23]. This calculation uses a rate equation that accounts for J/ψ breakup due to interactions with a dense comoving final-state medium. Additionally, the contribution from interactions with the spectator remnants is included. No assumption is made about the nature of the comoving medium, i.e., whether it is partonic or hadronic, only that it can be represented by a comover density and comover-J/ψ cross section σ_{co}, for which a value of 0.65 mb was found to match the NA50 data and then used for the projection to Au + Au at RHIC. The separate breakup cross section was taken to be $\sigma_{br} = 4.5$ mb. This value was taken from measurements in $p + A$ collisions at $\sqrt{s_{NN}} = 27.4/19.1$ GeV at the CERN SPS. Under the assumption that σ_{br} is energy independent, the value from those measurements was used until recently as the cold-nuclear-matter reference for heavy-ion collisions at $\sqrt{s_{NN}} = 17.2$ GeV [2], as well as in [22] as the reference for $\sqrt{s_{NN}} = 200$ GeV at RHIC.

However, the effective breakup cross section has now been shown to decrease significantly with collision energy [10]. In fact, a recent measurement in $p + A$ collisions at $\sqrt{s_{NN}} = 17.2$ GeV [9] yielded a value of $\sigma_{br} = 7.6 \pm 0.7 \pm 0.6$ mb with no antishadowing correction, and $\sigma_{br} = 9.3 \pm 0.7 \pm 0.7$ mb with antishadowing corrected for using EKS98 nuclear modified parton distribution functions (nPDFs). The value measured in $d + $Au collisions at RHIC [15] is $2.8^{+1.7}_{-1.4}$ mb after shadowing correction using EKS98, somewhat smaller than the 4.5 mb used in [22]. The corresponding calculation, shown in Fig. 6 as the black, dot-dot-dashed curve, significantly overestimated the suppression measured at midrapidity for Au + Au collisions at $\sqrt{s_{NN}} = 200$ GeV [5,7]. The suppression is stronger than the SPS case mainly due to the larger comover density calculated for RHIC.

An updated calculation [23] was then released that replaced the constant breakup cross section with a Bjorken-x-dependent function that goes to $\sigma_{br} = 0$ mb at $y = 0$, while the same $\sigma_{co} = 0.65$ mb was used for the comover interactions as before. Additionally, a J/ψ regeneration component was added that is normalized to the ratio of open charm production squared to J/ψ production in $p + p$ collisions. These results are also included in Fig. 6. The suppression from initial-state effects alone is much weaker at midrapidity than the previous calculation, due to both the change in

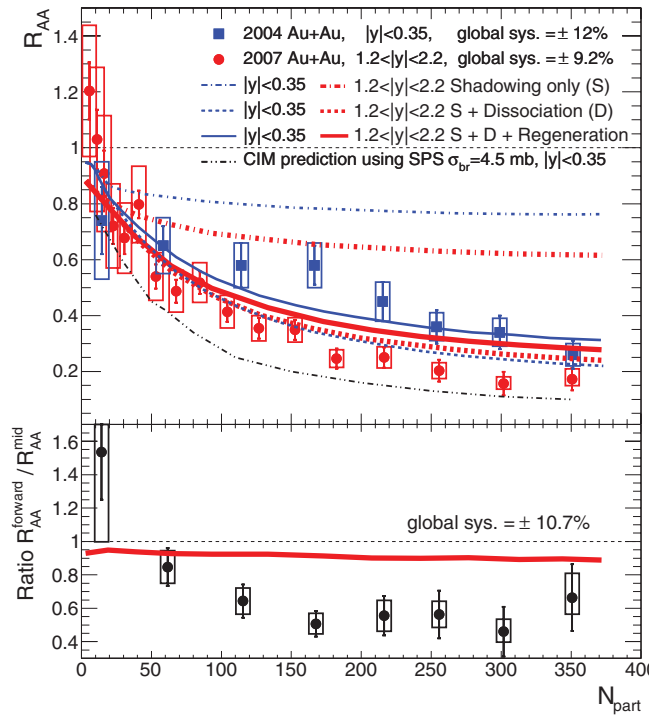

FIG. 6. (Color online) Measured J/ψ R_{AA} vs N_{part} from Fig. 3 compared to calculations within the comover interaction model [22,23]. The lower panel shows ratios of forward to midrapidity points and curves from the upper panel. The round (red) data points and thick (red) curves are for forward rapidity ($1.2 < |y| < 2.2$), while the square (blue) data points and thin (blue) curves are for midrapidity ($|y| < 0.35$). The lowest dot-dot-dashed (black) curve is the older CIM calculation [22] predicted from SPS data. The remaining curves are from the more recent calculations [23], where the dot-dashed curves are from shadowing alone, the dashed curves also include dissociation in the comoving medium, and the solid curves are the total effect after including J/ψs from regeneration.

$\sigma_{\rm br}$, as well as an updated parametrization of shadowing effects.

The CNM effects (i.e., shadowing and $\sigma_{\rm br}$) are much stronger at forward rapidity than midrapidity, due in part to the assertion that $\sigma_{\rm br}$ is negligible at midrapidity. On the other hand, the effects of comover dissociation and regeneration are stronger at midrapidity. The combination of these three effects leads to predictions which are overall very similar at forward and midrapidity (as seen in the lower panel).

C. Quark-gluon plasma and hadronic gas

The third model we compare with is from Zhao and Rapp [24,25]; it incorporates both a quark-gluon-plasma (QGP) phase and a hadronic-gas phase. In this calculation, they include two different models for CNM effects. In the first case, J/ψ-nucleon breakup is calculated in the usual Glauber formalism, in which shadowing plus anti-shadowing are assumed to roughly cancel, such that the overall shadowing effects are encapsulated in the breakup cross section $\sigma_{\rm br}$. p_T broadening is included via Gaussian smearing. In the second case, nuclear shadowing is added to the CNM effects. The rapidity-independent breakup cross section and the p_T broadening are handled as in the first case.

The thermal dissociation is modeled via a Boltzmann transport equation for both QGP and hadronic-gas phases. The QGP is assumed to be an isentropically expanding cylindrical fireball. J/ψ-medium interactions are assumed to stop at a freeze-out temperature of 120 MeV. The final J/ψ p_T distribution is calculated by spatially integrating the final phase-space distribution. For the regeneration component it is assumed that the $c\bar{c}$ is thermally equilibrated with the medium when it coalesces into a J/ψ. Consequently, the J/ψ p_T distribution is governed by a blast-wave equation for the transverse flow velocity. The normalization of this component is performed by plugging the initial charm densities into a rate equation with both gain and loss terms and solving at the freeze-out time.

The calculation results, using the second case for the CNM effects, are shown in Fig. 7, along with the separate dissociation and regeneration components. Though the second cold-nuclear-matter case increases the suppression for more central events compared to the first scenario, the difference in the overall suppression between the two scenarios is small. The qualitative trends of the calculation agree with the experimental data; however, the calculated suppression is very similar between forward and midrapidity, which is in disagreement with the data.

It is noteworthy that the regeneration component is only slightly larger at midrapidity in this model than at forward rapidity. This is in contrast to other regeneration or recombination calculations that result in a significant narrowing of the J/ψ rapidity distribution in central Au + Au events (see, for example, [28,29]). In simple calculations, the J/ψ recombination contribution scales as the square of the local charm density $[(dN_{c\bar{c}}/dy)^2]$ and thus there is substantially less recombination at forward rapidity. This modeling also

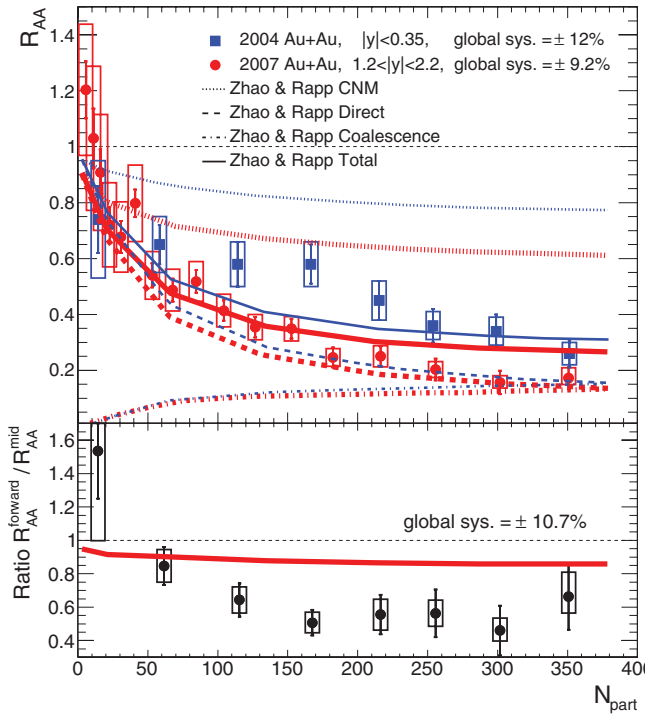

FIG. 7. (Color online) Measured J/ψ $R_{\rm AA}$ vs $N_{\rm part}$ from Fig. 3 compared to calculations by Zhao and Rapp [24,25]. The lower panel shows ratios of forward to midrapidity points and curves from the upper panel. The round (red) data points and dashed (red) curves are for forward rapidity ($1.2 < |y| < 2.2$), while the square (blue) data points and solid (blue) curves are for midrapidity ($|y| < 0.35$). The calculations incorporate cold- and hot-nuclear-matter suppression, as well as coalescence of $c\bar{c}$ pairs. The various curves represent the different contributions or the total as indicated in the legend.

leads to predictions of significantly larger recombination enhancements at the LHC where charm production is much larger. However, in this calculation [25] with a full space-momentum distribution of charm pairs, the probability of a charm quark from one $c\bar{c}$ pair recombining with an anticharm quark from another $c\bar{c}$ pair is suppressed because they are typically spatially separated, which is then maintained through collective flow. Thus, their recombination is dominated by the case where a $c\bar{c}$ is produced as a pair that would normally not form a J/ψ but due to scattering in the medium have a reinteraction and recombine. In this case, the regeneration contribution has a rapidity dependence similar to that of the directly produced J/ψ.

D. Shadowing-nuclear absorption and initial-state energy loss

In addition to the above three models, we use a framework for calculating just the CNM effects and extrapolating them to Au + Au collisions. We begin with the prescription in [27] for d + Au collisions, which combines effects of nPDFs using the EPS09 parametrization [26] with a rapidity-independent J/ψ-nucleon breakup cross section $\sigma_{\rm br}$, along

with the possibility of initial-state parton energy loss. We have extended these calculations to the Au + Au case using the identical code. The EPS09 nPDFs reflect only the modification integrated over the nucleus. No information is available about the impact-parameter dependence. In the calculations presented here, the EPS09 modification is arbitrarily assumed to have a linear dependence on the longitudinal integrated nuclear thickness at the location of the nucleon-nucleon collision.

Figure 8(a) shows the projected CNM effect from these two contributions. The bands show the J/ψ results at (light, green) midrapidity and (dark, magenta) forward rapidity from all 31 EPS09 nPDF variations for $\sigma_{\rm br} = 0$, 3, 6, and 9 mb. Note that a value of $\sigma_{\rm br}$ greater than 6 mb (9 mb) is required to approach the data at midrapidity (forward rapidity), but the centrality dependence is still not reproduced. The lower panels show ratios for forward to midrapidity data points and all 31 EPS09 nPDFs for the four $\sigma_{\rm br}$. No combination of these two effects reproduces the modification in the rapidity shape for midcentral to central Au + Au collisions. One reason for the modest rapidity dependence is that at forward rapidity the J/ψ production results from one low-x gluon (in the nPDF shadowing regime) and one high-x gluon (in the nPDF antishadowing regime) and the two effects largely cancel.

As discussed in [27], one can attempt to improve the CNM calculation agreement with the d + Au data by including a parametrization of initial-state parton energy loss. Figure 8(b) shows results for all 31 EPS09 nPDF parametrizations and the four $\sigma_{\rm br}$ values with quadratic-length-dependent initial-state parton energy loss that best matched the d + Au data. The initial-state parton energy loss has a minimal effect over this rapidity range, which is not unexpected since the effect only becomes significant in d + Au for rapidity $y > 1.8$.

We note that this CNM calculation does not give a full description of the d + Au data, adding some uncertainty to its use in Au + Au collisions. Nevertheless, it is informative that the calculation clearly fails to simultaneously explain the Au + Au data at forward and midrapidity. We observe J/ψ suppression beyond that expected from the CNM effects included in this calculation with the choice of a reasonable value of 3.0–3.5 mb for $\sigma_{\rm br}$ at RHIC.

E. p_T dependence of the suppression

Most of the above calculations do not include predictions for the J/ψ suppression as a function of transverse momentum. However, the calculation of Zhao and Rapp [25] provides

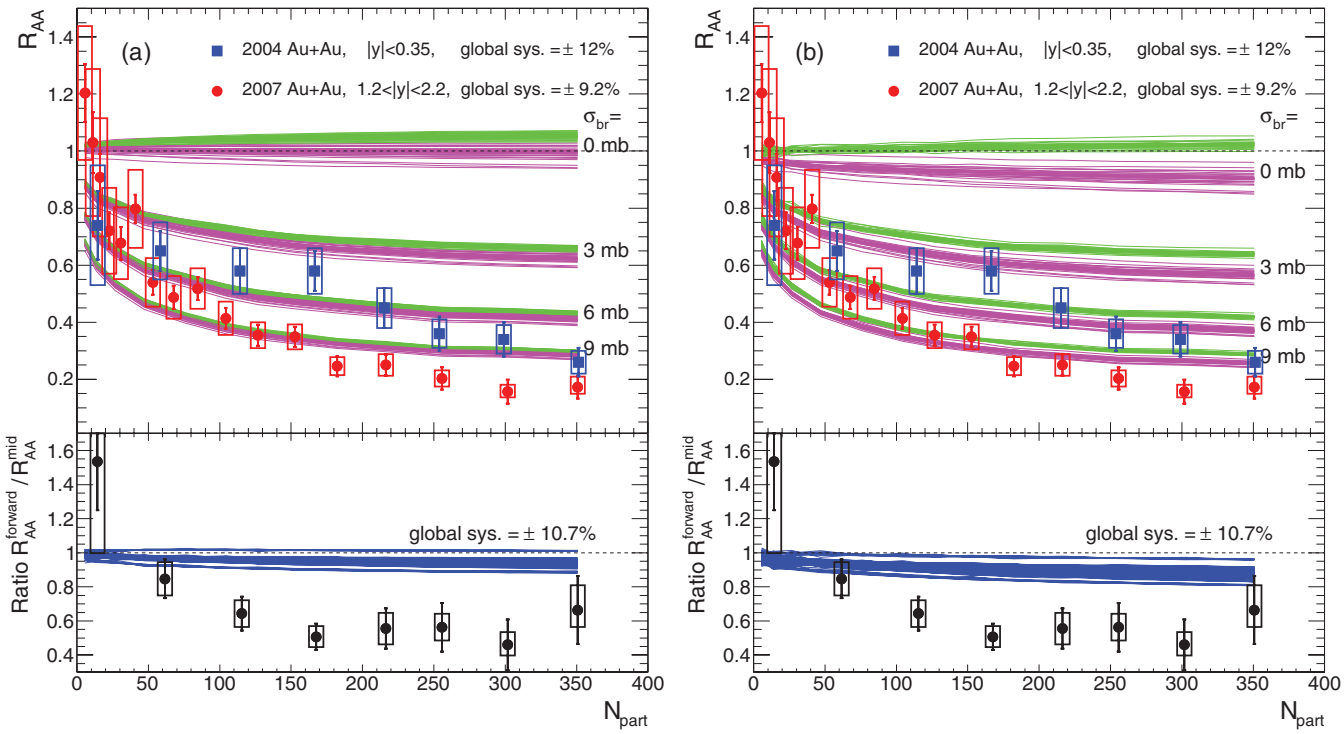

FIG. 8. (Color online) Measured J/ψ $R_{\rm AA}$ vs $N_{\rm part}$ from Fig. 3 compared to EPS09 calculations [26], following the prescription in [17,27]. The lower panels show ratios of forward to midrapidity points and curves from the upper panels. The round (red) data points and darker (magenta) curves are for forward rapidity ($1.2 < |y| < 2.2$), while the square (blue) data points and lighter (green) curves are for midrapidity ($|y| < 0.35$). The calculations include cold-nuclear-matter effects (nPDF and $\sigma_{\rm br}$) (a) not including and (b) including initial-state parton energy loss with a quadratic length dependence and a chosen strength that most closely matches the d + Au data, as detailed in [27]. The calculations are for all 31 EPS09 [26] nPDF variations and the labeled value for $\sigma_{\rm br} = 0$, 3, 6, and 9 mb. See text for details, but note in the lower panels that for all cases the various $\sigma_{\rm br}$ values result in (a) less than 10% or (b) less than 20% differences between forward and midrapidity modifications, whereas the data ratios indicate considerably larger differences.

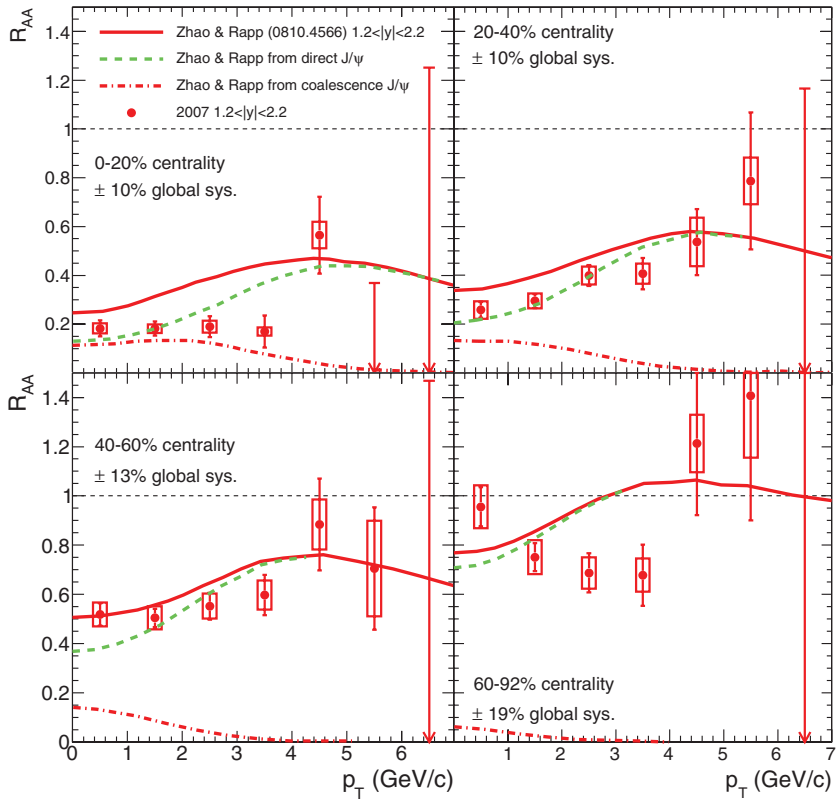

FIG. 9. (Color online) Measured J/ψ $R_{\rm AA}$ vs p_T for the four indicated centrality bins at forward rapidity, as in Fig. 4. The curves are model calculations by Zhao and Rapp from [24,25], which incorporate cold- and hot-nuclear-matter suppression as well as coalescence of $c\bar{c}$ pairs.

nuclear modification factors at both midrapidity and forward rapidity as a function of p_T. Shown in Fig. 9 are the results compared with our experimental data. Their calculations indicate a moderate rise in $R_{\rm AA}$ versus p_T predominantly due to the Cronin effect [32]. In fact, in other recombination models the enhancement is limited to low p_T [28], and in this calculation the recombination contribution drops off beyond $p_T \gtrsim 3$ GeV/c. At low p_T in the most central bin, the suppression from this calculation is too weak by up to a factor of 2.

More recently, Zhao and Rapp [30,31] have modified this calculation to include feed-down from B mesons and a reduced suppression at higher p_T due to the longer formation time of the preresonance state to the J/ψ from time dilation. These contributions serve to increase $R_{\rm AA}$ at higher p_T compared to the previous calculation and are compared to the forward rapidity data in Fig. 10. The current lack of statistics in the data at $p_T > 5$ GeV/c precludes a confirmation of this effect.

It should also be noted that, in the new calculation by Zhao and Rapp, CNM effects are handled differently than in the earlier calculation. An effective breakup cross section of 3.5 (5.5) mb at $y = 0$ (1.7) is used to account for the combined effects of shadowing and breakup. These effective cross sections are obtained from comparison with recent PHENIX $d+$Au data. They argue that the larger effective breakup cross section at forward rapidity is most likely associated with shadowing effects, and thus it causes a suppression of the number of charm pairs relative to midrapidity. Therefore, the additional effective absorption at forward rapidity is associated with a reduction in the yields of open charm as well as the J/ψ, thereby also reducing the J/ψ regeneration contribution. It is important to note that the resulting hot-nuclear-matter suppression in this calculation is very similar at midrapidity and forward rapidity. The new calculation produces a forward rapidity to midrapidity $R_{\rm AA}$ ratio of about 0.7 in central collisions, which is in better agreement with the data. This is due almost entirely to including cold-nuclear-matter effects

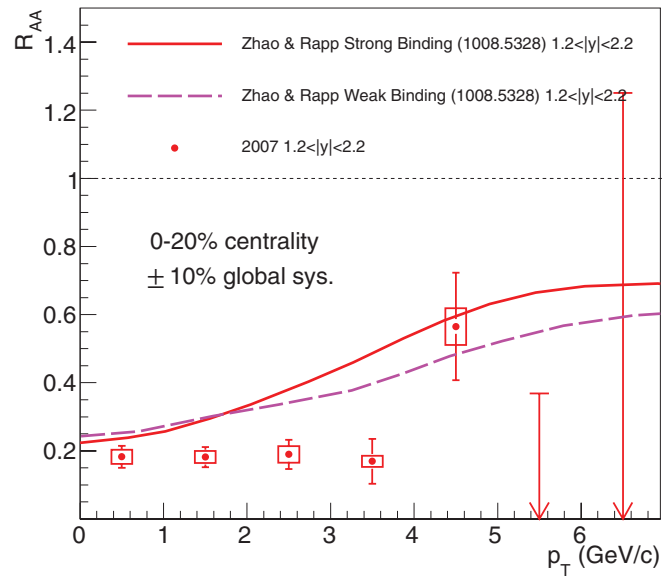

FIG. 10. (Color online) Measured J/ψ $R_{\rm AA}$ vs p_T for 0%–20% centrality at forward rapidity. The curves are from more recent calculations by Zhao and Rapp [30,31].

with a strong rapidity dependence, as reflected in the $d + \mathrm{Au}$ data. A second model of interest to the p_T dependence of J/ψ production is the so-called hot-wind model [33]. This model predicts a decrease in J/ψ R_{AA} at higher p_T in semicentral events, based on a modification of the screening length due to the relative velocity between the J/ψ and the medium. However, there is no quantitative calculation available at forward rapidities, and there is no evidence for such an effect in the p_T range covered by the present data.

V. SUMMARY AND CONCLUSIONS

We have presented new and more precise measurements of J/ψ nuclear modification at forward rapidity in $\mathrm{Au} + \mathrm{Au}$ collisions at $\sqrt{s_{NN}} = 200$ GeV. The results confirm our earlier published findings of a larger suppression at forward compared with midrapidity. This, combined with the similar suppression of J/ψ at midrapidity between RHIC and lower energy measurements, remains an outstanding puzzle in terms of a full theoretical description.

Due to the lack of a comprehensive and consistent understanding of the numerous cold-nuclear-matter effects and their extrapolation to nucleus-nucleus collisions, extracting a quantitative measurement of the hot-nuclear-matter effects is not possible at the present time. However, it is clear that part of the observed suppression is attributable to hot-nuclear-matter effects, as the suppression in $\mathrm{Au} + \mathrm{Au}$ collisions is larger than predicted by the current models of CNM effects. It will be useful for all calculations to include the transverse momentum dependence for future comparisons, especially as the experimental uncertainties, particularly at high p_T, will only improve in the future.

ACKNOWLEDGMENTS

We thank the staff of the Collider-Accelerator and Physics Departments at Brookhaven National Laboratory and the staff of the other PHENIX participating institutions for their vital contributions. We acknowledge support from the Office of Nuclear Physics in the Office of Science of the Department of Energy, the National Science Foundation, a sponsored research grant from Renaissance Technologies LLC, Abilene Christian University Research Council, Research Foundation of SUNY, and Dean of the College of Arts and Sciences, Vanderbilt University (U.S.A), Ministry of Education, Culture, Sports, Science, and Technology and the Japan Society for the Promotion of Science (Japan), Conselho Nacional de Desenvolvimento Científico e Tecnológico and Fundação de Amparo à Pesquisa do Estado de São Paulo (Brazil), Natural Science Foundation of China (P. R. China), Ministry of Education, Youth and Sports (Czech Republic), Centre National de la Recherche Scientifique, Commissariat à l'Énergie Atomique, and Institut National de Physique Nucléaire et de Physique des Particules (France), Ministry of Industry, Science and Tekhnologies, Bundesministerium für Bildung und Forschung, Deutscher Akademischer Austausch Dienst, and Alexander von Humboldt Stiftung (Germany), Hungarian National Science Fund, OTKA (Hungary), Department of Atomic Energy and Department of Science and Technology (India), Israel Science Foundation (Israel), National Research Foundation and WCU program of the Ministry Education Science and Technology (Korea), Ministry of Education and Science, Russian Academy of Sciences, Federal Agency of Atomic Energy (Russia), VR and the Wallenberg Foundation (Sweden), the U.S. Civilian Research and Development Foundation for the Independent States of the Former Soviet Union, the US-Hungarian Fulbright Foundation for Educational Exchange, and the US-Israel Binational Science Foundation.

[1] T. Matsui and H. Satz, Phys. Lett. B **178**, 416 (1986).
[2] M. Abreu *et al.* (NA50 Collaboration), Phys. Lett. B **477**, 28 (2000).
[3] D. Kharzeev, C. Lourenco, M. Nardi, and H. Satz, Z. Phys. C **74**, 307 (1997).
[4] U. W. Heinz and M. Jacob, arXiv:nucl-th/0002042.
[5] A. Adare *et al.* (PHENIX Collaboration), Phys. Rev. Lett. **98**, 232301 (2007).
[6] J. L. Nagle (PHENIX Collaboration), arXiv:0705.1712 (2007).
[7] H. Pereira Da Costa (PHENIX Collaboration), Nucl. Phys. A **774**, 747 (2006).
[8] B. Alessandro *et al.* (NA50 Collaboration), Eur. Phys. J. C **33**, 31 (2004).
[9] R. Arnaldi (NA60 Collaboration), Nucl. Phys. A **830**, 345c (2009).
[10] C. Lourenco, R. Vogt, and H. K. Woehri, J. High Energy Phys. 02 (2009) 014, and references therein.
[11] K. Adcox *et al.* (PHENIX Collaboration), Nucl. Instrum. Methods A **499**, 469 (2003).
[12] M. Allen *et al.* (PHENIX Collaboration), Nucl. Instrum. Methods A **499**, 549 (2003).
[13] H. Akikawa *et al.* (PHENIX Collaboration), Nucl. Instrum. Methods A **499**, 537 (2003).
[14] M. L. Miller, K. Reygers, S. J. Sanders, and P. Steinberg, Annu. Rev. Nucl. Part. Sci. **57**, 205 (2007).
[15] A. Adare *et al.* (PHENIX Collaboration), Phys. Rev. C **77**, 024912 (2008).
[16] R. Brun *et al.*, CERN Program Library Long Write-up W5013 (1994), [http://wwwasd.web.cern.ch/wwwasd/geant/].
[17] A. Adare, Phys. Rev. Lett. **107**, 142301 (2011).
[18] A. Milov *et al.*, J. Phys. G **34**, S701 (2007).
[19] D. Kharzeev, E. Levin, M. Nardi, and K. Tuchin, Nucl. Phys. A **826**, 230 (2009).
[20] K. Tuchin, Nucl. Phys. A **854**, 198 (2011).
[21] M. Nardi, Nucl. Phys. A **855**, 392 (2011).
[22] A. Capella and E. G. Ferreiro, Eur. Phys. J. C **42**, 419 (2005).
[23] A. Capella, L. Bravina, E. G. Ferreiro, A. B. Kaidalov, K. Tywoniuk, and E. Zabrodin, Eur. Phys. J. C **58**, 437 (2008).
[24] X. Zhao and R. Rapp, Phys. Lett. B **664**, 253 (2008).
[25] X. Zhao and R. Rapp, Eur. Phys. J. C **62**, 109 (2009).
[26] K. J. Eskola, H. Paukkunen, and C. A. Salgado, J. High Energy Phys. 04 (2009) 065.

[27] J. L. Nagle, A. D. Frawley, L. A. Linden Levy, and M. G. Wysocki, Phys. Rev. C **84**, 044911 (2011).
[28] R. L. Thews and M. L. Mangano, Phys. Rev. C **73**, 014904 (2006).
[29] K. Zhou, N. Xu, and P. Zhuang, Nucl. Phys. A **834**, 249C (2010).
[30] X. Zhao and R. Rapp, Phys. Rev. C **82**, 064905 (2010).
[31] X. Zhao (private communication).
[32] D. Antreasyan, J. W. Cronin, H. J. Frisch, M. J. Shochet, L. Kluberg, P. A. Piroué, and R. L. Sumner, Phys. Rev. D **19**, 764 (1979).
[33] H. Liu, K. Rajagopal, and U. A. Wiedemann, Phys. Rev. Lett. **98**, 182301 (2007).